Article

Visualization of Optical Vortex Forces Acting on Au Nanoparticles Transported in Nanofluidic Channels

Kichitaro Nakajima, Tempei Tsujimura, Kentaro Doi, and Satoyuki Kawano*

ACCESS | Metrics & More | Article Recommendations | SI Supporting Information

ABSTRACT: The optical manipulation of nanoscale objects via structured light has attracted significant attention for its various applications, as well as for its fundamental physics. In such cases, the detailed behavior of nano-objects driven by optical forces must be precisely predicted and controlled, despite the thermal fluctuation of small particles in liquids. In this study, the optical forces of an optical vortex acting on gold nanoparticles (Au NPs) are visualized using dark-field microscopic observations in a nanofluidic channel with strictly suppressed forced convection.

Manipulating Au NPs with an optical vortex allows the evaluation of the three optical force components, namely, gradient, scattering, and absorption forces, from the in-plane trajectory. We develop a Langevin dynamics simulation model coupled with Rayleigh scattering theory and compare the theoretical results with the experimental ones. Experimental results using Au NPs with diameters of 80−150 nm indicate that our experimental method can determine the radial trapping stiffness and tangential force with accuracies on the order of 0.1 fN/nm and 1 fN, respectively. Our experimental method will contribute to broadening not only applications of the optical-vortex manipulation of nano-objects, but also investigations of optical properties on unknown nanoscale materials via optical force analyses.
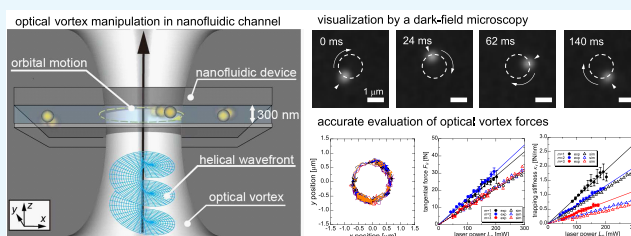
INTRODUCTION

Optical tweezers are promising for applications in nanotechnology and have attracted wide attention since Ashkin succeeded in manipulating microparticles using a Gaussian beam.[1−3] The accurate evaluation and control of the optical forces acting on nanoscale objects are important to effectively apply optical tweezers to nanotechnology. In nanoscale applications, most target objects are biological particles or molecules such as viruses,[4,5] proteins,[6] and nucleic acids,[7] which are usually treated as suspensions or solutions in analytical processes. In such a situation, the liquid flow prevents an accurate evaluation of the optical forces acting on the targets because the target motion is drifted by the forced convection. Especially in nanoscale or microscale spaces, subtle disturbances in a liquid, such as a pressure distribution or a local temperature change, induce the liquid flow in a test section, which can be a dominant factor governing the target motion.[8]

There are several difficulties involved in the quantitative evaluation of optical forces in liquids as a result of nonignorable environmental perturbations, such as convective heat transfer, mass transfer, and thermal fluctuations. In previous studies,[9−13] we investigated the transport phenomena of micro- and nanoparticles in liquids, where the optical forces were measured using microfluidic and nanofluidic channels that were finely tuned to confine the target particles in narrow spaces. We also developed theoretical models and performed numerical simulations to ensure quantitative accuracy; these

simulations reproduced the actual spatiotemporal scales well. We found that Langevin dynamics simulations coupled with externally applied force fields could be used to reproduce the transport phenomena of small particles and biomacromolecules in liquids.[9−11] Nito et al.[12] experimentally and theoretically evaluated optical tweezers for polystyrene (PS) microparticles from the viewpoint of Ashkin's ray optics model,[14] where the effects of liquid flow and heat are highly suppressed in microchannels. Tsuji et al.[13] experimentally and numerically investigated the collective orbital motion of plural PS microparticles driven by an optical vortex by considering the hydrodynamic interactions between particles. We have demonstrated that optical forces can be tuned to manipulate small objects for various applications.[15,16] Recently, our research group[15,16] reported that the electrical measurement accuracy of micro- and nanoparticles is drastically improved when using an optical vortex that iteratively brings target particles into a double-slit test section. In the previous studies, we succeeded in manipulating single PS particles[15] and gold nanoparticles (Au NPs)[16] in a narrow space. However, the
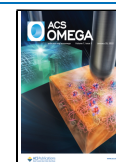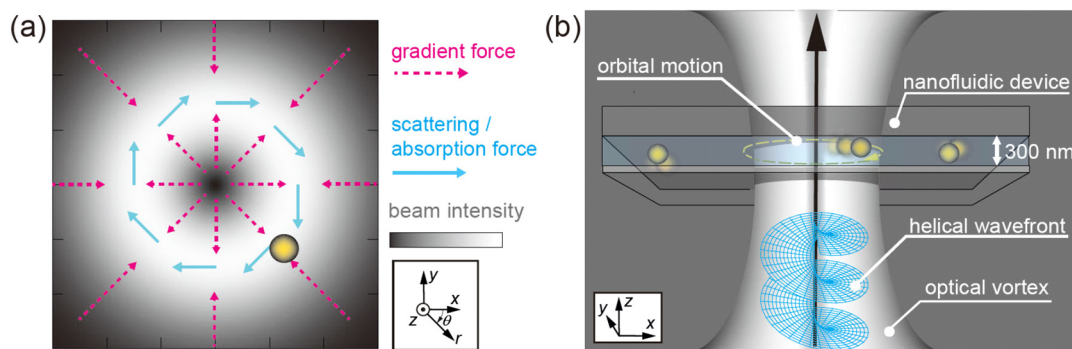
Figure 1. (a) Optical vortex forces acting on the gold nanoparticles (Au NPs) at the focal plane of the Laguerre−Gaussian (LG) beam. The radial gradient force traps the target particles in a ring-shaped orbit (magenta dotted arrows). The scattering and absorption forces act as a tangential force in the azimuthal direction, driving the orbital motion of the Au NP (blue arrows). (b) Schematic illustration of the particle tracking analysis of in-plane orbital motion in a nanofluidic channel with a height of ≈300 nm. The LG beam is made incident to drive the orbital motion of the Au NP. The Brownian motion along the z direction is restricted by the channel walls, which allows continuous visualization via dark-field microscopy. In the test section, the forced convection of surrounding liquid is highly suppressed by the nanofluidic structure.

reproducible manipulation of single nanoparticles is challenging because of the large thermal fluctuations and the small optical forces, which are on the order of 10^{-15} N (1 fN). Although accurate analyses of single-nanoparticle motion driven by an optical vortex are crucial to broadening its applications, the lack of reliable experimental methods prevents quantitative evaluations of the optical forces acting on Au NPs.

In this study, we focus on an experimental methodology to accurately investigate the optical forces acting on Au NPs using optical vortices, i.e., Laguerre−Gaussian (LG) beams,[17−20] which have been adopted for various applications.[15,16,21,22] We developed a nanofluidic channel that enabled the reproducible manipulation of single Au NPs and analyzed the optical forces acting on Au NPs with diameters of 80−150 nm without disturbance from a liquid flow. The nanofluidic channel is structured to diminish the forced convection in the test section, within which the nano-objects are analyzed for motion caused by the optical forces. Furthermore, the nanofluidic channel confines the target particles to a microscopic observation focal plane, allowing continuous visualization of the target motion. Using the nanofluidic channel, we observed the in-plane motion of Au NPs via dark-field microscopy and analyzed the optical forces acting on Au NPs. The optical force analysis was systematically conducted with various laser powers, topological charges of the optical vortex beam, and particle diameters. The experimental results were compared with those of numerical simulation based on the Langevin dynamics and Rayleigh scattering theory.[23,24] The experimental and theoretical results showed quantitative agreement, demonstrating that the established method can effectively and accurately analyze the nanoparticle motion caused by optical vortex forces. Additionally, our method can contribute to accurate predictions of the optical parameters, such as the complex refractive index, polarizability, and optical cross sections of unknown nanoscale materials via optical force analyses.

RESULTS AND DISCUSSION

Accurate Force Measurement Using an Optical Vortex and Nanofluidic Channel. LG beams were adopted to drive Au NP motion since they allow us to simultaneously investigate three optical forces: gradient, scattering, and absorption forces. In addition to the gradient force, the scattering and adsorption forces contribute to the in-plane particle motion induced by an LG beam,[25,26] which allows us to analyze the fraction of the three components in the trajectory. LG beam irradiation induces a Au NP orbital motion (Figure 1a), where the gradient force works along the radial direction as a result of interaction between the oscillating electric field and an electric dipole caused by an incident light and a Au NP, respectively. The gradient force traps target particles in a ring-shaped orbit (magenta dotted arrows in Figure 1a). Furthermore, based on the momentum conservation law, the scattering and absorption forces act along the azimuthal direction due to the momentum transfer via the scattering and absorption processes from the incident light to the Au NP. These forces drive the orbital motion of Au NP (blue arrows in Figure 1a). Generally, investigations of the scattering and absorption forces require special microscopic setups, which can observe an out-of-plane motion of the target particles;[27,28] however, LG beams allow us to analyze the scattering and absorption forces with the gradient force using an in-plane particle tracking analysis.[12,13] The in-plane particle tracking was performed using a nanofluidic channel, as shown in Figure 1b. The nanofluidic channel with a channel height of 300 nm confines the Au NPs to the focal plane of dark-field microscopy. The lower the channel height, the better it is at preventing forced convection; however, the channel height was optimized for the microscopic observation in this study. The observations were conducted with a frame rate of 1000 fps. The tangential force and the radial trapping stiffness, which are attributed to the scattering and absorption forces and the gradient force, respectively, were independently evaluated via the in-plane particle tracking.

Construction of the Nanofluidic Channel. We fabricated the nanofluidic channel, as schematically illustrated in Figure 2a. The channel comprised three parts: (i) a microfluidic channel with the height of 10 μm for introducing Au NPs into the nanofluidic channel, which works as both an inlet and an outlet for the Au NP suspension; (ii) a nanofluidic channel with many small pillars to diminish the forced convection in the test section; (iii) a nanofluidic channel with four large pillars for the test section, where the motion of the Au NP was analyzed via particle tracking. The large pillars placed in the test section keep the channel from collapsing. It should be noted that contact with a solid wall is resistant to liquid flow due to friction. The small pillars increase the
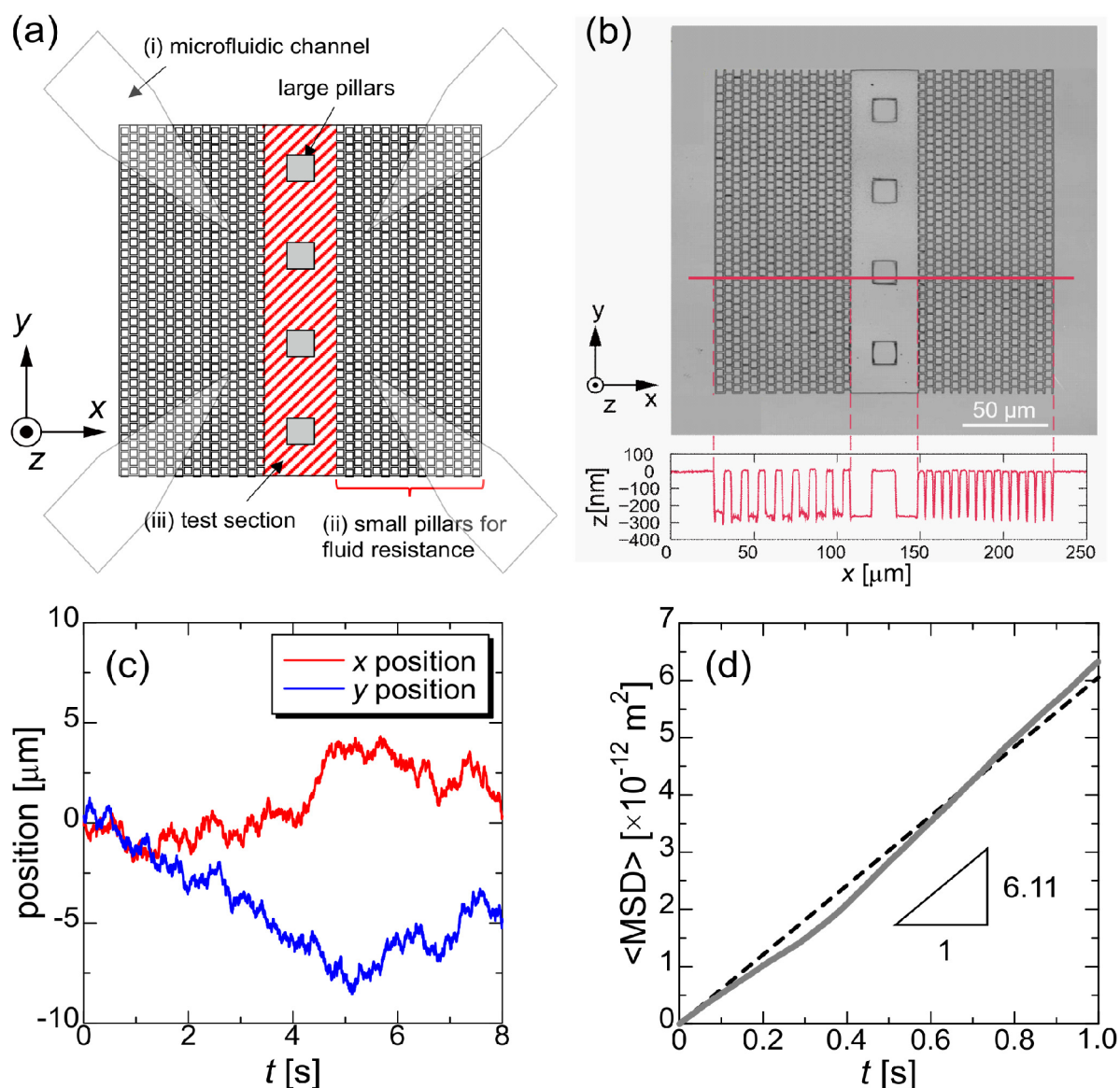
Figure 2. (a) Schematic of the nanofluidic channel. (b) Micrograph of the nanofluidic channel acquired using a laser microscope (OLS4100, Olympus, Japan) and its depth profile, which indicates that the channel depth is ≈300 nm. (c) Trajectory of the Brownian motion of a 150 nm Au NP in the nanofluidic channel, showing that there is no drift motion toward a specific direction caused by the forced convection in the test section. (d) Mean square displacement (MSD) analysis of the Brownian motion shown in panel (c).

contact surface area between the liquid and channel wall, which results in the great reduction of the liquid flow in the test section, as discussed below. Figure 2b represents a micrograph of the pattern of the nanofluidic channel. Figure S1 shows the detailed information concerning the channel dimensions.

To evaluate the visualization capabilities of the nanofluidic channel, we first observed the Brownian motion of Au NPs with a diameter of 150 nm in the channel whose height is ≈300 nm. The Brownian motion of the target particle was continuously visualized for 10 s. The particle position randomly fluctuated without any drift toward a specific direction (Figure 2c), suggesting that the forced convection of the surrounding liquid was fully suppressed in the test section by the nanofluidic structure (Figure 2b). The reduction of the forced convection was supplementarily discussed in detail in the SI Appendix 1. The diffusion coefficient of the Brownian motion, D, was evaluated to validate the accuracy of

the particle tracking analysis. The ensemble average of the mean square displacement (MSD) of the particle was calculated from the acquired trajectory such that MSD = $\langle (\mathbf{x}_p(t) - \mathbf{x}_p(0))^2 \rangle$, where $\mathbf{x}_p(t)$ is the particle position at a time t. Figure 2d indicates a linear increase in the MSD value with time. From the slope of the MSD curve, the D value of Au NPs with a diameter of 150 nm is $D = \text{MSD}/4t = 1.63 \times 10^{-12}$ m^2s^{-1}, which is on the same order of magnitude as the theoretical estimation according to the Stokes−Einstein relation, $D = k_B T/3\pi\mu d_p \approx 3.31 \times 10^{-12}$ m^2s^{-1}. This demonstrates the capability of the nanofluidic channel to directly observe the motion of Au NPs without the influence of forced convection.

Visualization of the Orbital Motion in the Nanofluidic Channel. Next, we observed the orbital motion of a Au NP driven by the LG beam with a topological charge $m = 1$ and a laser power of $L_p = 135$ mW in the nanofluidic channel. Snapshots of the orbital motion of Au NPs with diameters of
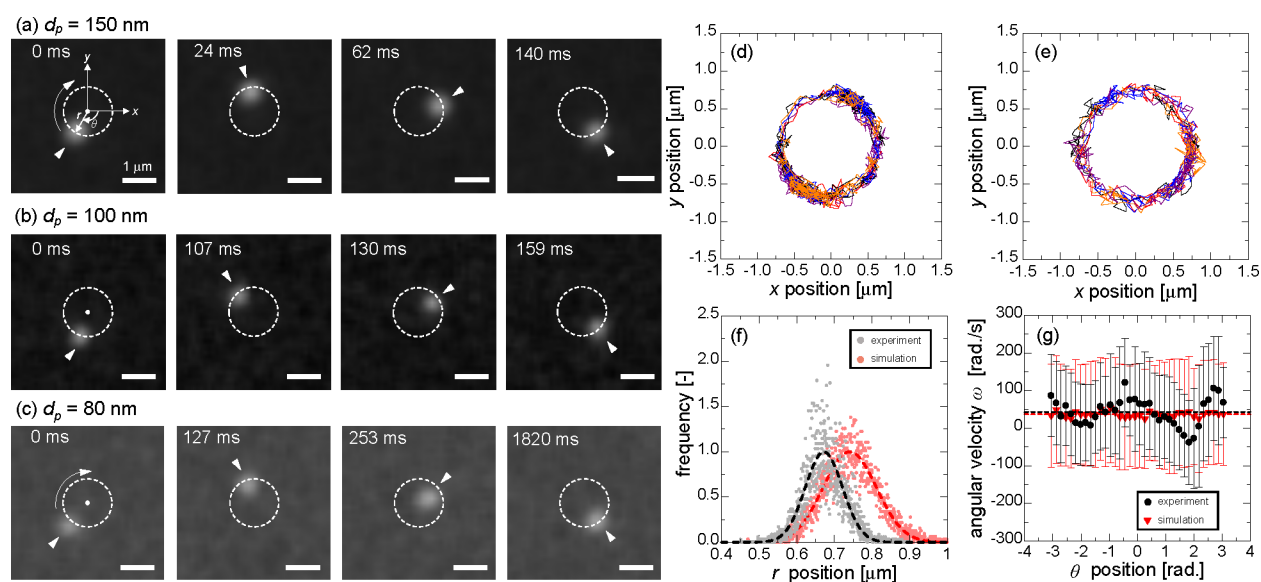
Figure 3. (a−c) Dark-field snapshots of the orbital motion of a Au NP with diameters of (a) 150 nm, (b) 100 nm, and (c) 80 nm. Scale bars denote 1 μm. (d,e) Trajectory of the orbital motion of a Au NP with a diameter of 100 nm obtained from (d) the experiment and (e) the numerical simulation. Each color corresponds to the orbital motion over one revolution, and five trajectories are represented. (f) Histograms of the radial position distribution of a 100 nm Au NP during the orbital motion. The vertical axis value is normalized such that the height of the fitted Gaussian curve is 1. (g) Angular velocity dependency on the angular position for a 100 nm Au NP. The angular velocity, ω_i, is written as $(\omega_i = (\theta(t_i) - \theta(t_{i-1}))/\Delta t$, where $\theta(t_i)$ and Δt = 1 ms are the angular position at time t_i and the time interval between individual snapshots, respectively. The error bars denote the standard deviation of the angular velocity at each point and are attributed to the Brownian motion along the azimuthal direction.

150, 100, and 80 nm are shown in Figure 3a−c, respectively. A Au NP rotated in a clockwise manner in a ring-shaped orbit. The particle tracking analysis was applied to reveal the trajectory of the orbital motion of a 100 nm Au NP (Figure 3d). We also numerically calculated the orbital motion of a 100 nm Au NP under the same conditions of the experiments (Figure 3e). Here, it should be noted that the experimental particle trajectories were slightly distorted from the circular orbit; i.e., the trajectories showed elliptic orbits. However, the degree of distortion was sufficiently low, and the effect on the analysis results of the optical forces was negligible, as discussed in the SI Appendix 2.

Both the experimental and numerical trajectories implied that the radial positions of a Au NP thermally fluctuated with Brownian motion in a ring-shaped orbit around an equilibrium orbital radius, r_t (Figure 3f). We calculated this orbital radius from the average of the radial position. Gauss functions with averages and standard deviations of r_t and σ, i.e., $G(r) = \exp[-(r - r_t)^2/2\sigma^2]$, are depicted via histograms (Figure 3f). The experimental and numerical histograms showed Gaussian distributions with orbital radii of $r_t = 6.72 \times 10^{-1}$ and 7.44×10^{-1} μm, respectively. Although the orbital radii showed good agreement between the experimental and numerical results, there was an ≈10% error. This error is attributed to the fact that the transverse intensity distribution of the LG beam depends on the z-position of the objective lens in the experiment. The lens position was set to clearly visualize the particle image and was slightly different from the theoretical focal plane of the LG beam because of the chromatic aberration between the incident laser (λ = 1064 nm) and the observation light (visible light). This difference contributed to the discrepancy between the experimental and numerical orbital radii.

As the other aspect of the histogram, σ is correlated with the trapping stiffness, κ_r, on the basis of the relationship $\kappa_r = k_B T/$

σ^2.[29] Under these laser irradiation conditions, the experimental and numerical trapping stiffness were calculated to be κ_r = 1.33 and 0.81 fN·nm^{-1}, respectively, showing a reasonable agreement.

The angular velocity, ω, was analyzed by tracking azimuthal positions of a Au NP (Figure 3e). The numerical result indicated a homogeneous angular velocity at each angular position. Although the experimental angular velocity depended on the angular position because of the imperfection of the optical system using LG beams,[13,30] the mean angular velocities, $\bar{\omega}$, showed good agreement for the experimental ($\bar{\omega}$ = 38.4 rads^{-1}) and numerical ($\bar{\omega}$ = 37.6 rads^{-1}) results. Thus, we used the mean angular velocity for the calculation of the tangential force F_θ, which consists of the scattering and absorption forces. Assuming a uniform circular motion with r_t and $\bar{\omega}$, the tangential force was computed using the Stokes drag force $F_\theta = 3\pi\mu d_p r_t \bar{\omega}$, which was 21.5 and 23.3 fN for the experimental and numerical results, respectively. The Langevin dynamics model coupled with the Rayleigh scattering theory predicted the optical vortex forces well. This finding will be useful for various applications of optical vortex manipulations of nanoparticles in liquids, e.g., electrical measurements of nanoparticles manipulated by an optical vortex.[16] We have also developed a variety of computational methods for optical manipulation techniques ranging from the Rayleigh regime[11,13] to Ashkin's ray optics[12] that predict experimental results well.

Systematic Investigation of Optical Vortex Forces Acting on Au NPs. Using the nanofluidic channel, we systematically investigated the orbital radius, tangential force, and radial trapping stiffness of the orbital motion of Au NPs by varying the laser power, topological charge, and particle diameter. Figure 4 shows the experimental and numerical results. In the experiments, we used Au NPs with diameters of 80, 100, and 150 nm. The laser power and topological charge were varied from 20 to 400 mW and from 1 to 3, respectively.
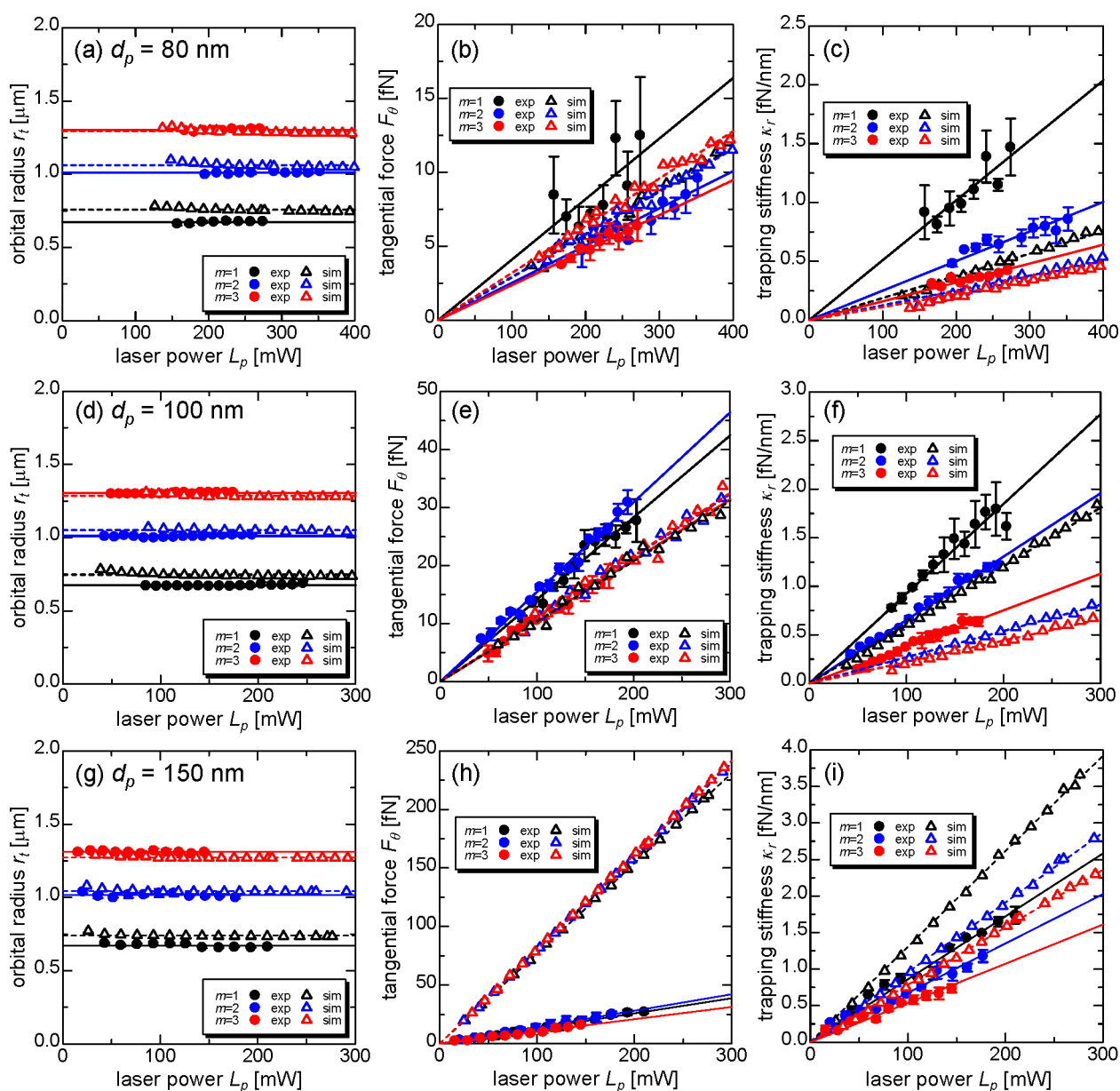
Figure 4. Systematic investigation of the optical vortex forces acting on the Au NPs. (a−c) Laser power, L_p, dependency of (a) the orbital radius r_t, (b) the tangential force F_θ, and (c) the trapping stiffness κ_r of the orbital motion of Au NPs with a diameter of 80 nm. (d−f) Laser power dependency of (d) the orbital radius, (e) the tangential force, and (f) the trapping stiffness of the orbital motion of Au NPs with a diameter of 100 nm. (g−i) Laser power dependency of (g) the orbital radius, (h) the tangential force, and (i) the trapping stiffness of the orbital motion of Au NPs with a diameter of 150 nm.

For all the Au NP diameters, the orbital radius was constant for the various laser powers, as shown in Figure 4a,d, and g, because the orbital radius only depends on the transverse intensity distribution of the incident LG beam, not merely on its intensity. Conversely, the tangential force and the trapping stiffness showed a positive linear correlation with the laser power for all particle diameters, consistent with eqs 2 and 3. For each condition, we succeeded in measuring changes in the optical vortex forces on the order of 1 fN for the tangential force and on the order of 0.1 fNnm^{-1} for the trapping stiffness caused by the change in the laser power; this demonstrates the analysis accuracy using the nanofluidic channel.

The accuracy of the acquired parameters using the nanofluidic channel was further confirmed by comparing the experimental and numerical results (Table 1). The orbital

radius was evaluated by the least-squares fit for each condition, and the experimental results for the orbital radius agreed with the numerical results, indicating that a spatial resolution of 100 nm or more is preferable for the particle tracking analysis.

In the d_p = 80 and 100 nm cases, the tangential force showed a good agreement for the experimental and numerical results, demonstrating that the particle tracking analysis using the nanofluidic channel can evaluate scattering and absorption forces with an accuracy on the order of 1 fN. Conversely, in the case of d_p = 150 nm, there is a large discrepancy between the tangential forces in the experimental and numerical results (Figure 4h). As discussed below, this discrepancy is not an error in the measurement but rather indicates an intrinsic limitation of the Rayleigh approximation for larger Au NPs. Our experimental method using the nanofluidic channel

Table 1. Comparison between the Experimental and Numerical Results of the Systematic Investigation of the Optical Vortex Forces Acting on the Au NPs[a]

| conditions		exp./sim. [-]		
d_p [nm]	m	r_t	F_θ	κ_r
80	1	0.89	1.40	2.70
	2	0.95	0.87	1.99
	3	1.01	0.74	1.44
100	1	0.90	1.36	2.43
	2	0.96	1.44	2.42
	3	1.01	0.67	1.71
150	1	0.91	0.21	0.66
	2	0.97	0.18	0.71
	3	1.03	0.13	0.68

[a]The ratio between experimental and numerical results is defined as follows: the ratio of the orbital radius r_t was obtained from the least-squares fitting shown in Figure 4a,d, and g. The ratios of the tangential force and trapping stiffness were obtained from the slopes of the fitted lines in Figure 4b,c,e,f,h, and i.

succeeded in accurately analyzing the tangential force driving the orbital motion. This implies that our method can contribute to investigations of the optical scattering and absorption cross sections of nano-objects.

The trapping stiffness showed values on the same order for both the experimental and numerical results, as shown in Figure 4c,f, and i, indicating that direct observations of thermal fluctuation of Au NPs in the optical-vortex force field

succeeded in accurately evaluating the radial optical-force component acting on the Au NPs. Although this measurement required a particle tracking accuracy on the order of 10 nm without external disturbances, the accurate tracking of Au NPs with particle diameters of less than 100 nm was achieved as a result of the continuous observation and the suppression of forced convection enabled by the nanofluidic channel, allowing the trapping stiffness to be analyzed with an accuracy on the order of 0.1 fNnm^{-1}.

Although several studies have contributed to establishing an experimental method to accurately measure optical forces, most of these have focused on experiments using micro-particles.[31−34] In microscale measurements, the optical forces acting on the target particles were typically greater than 1 pN, much larger than those acting on nanoscale objects. Regarding nanoscale research, although theoretical studies are largely spread, infinitesimal optical forces acting on nanoscale (d_p < 100 nm) particles often fail to overcome thermal fluctuations, preventing researchers from experimentally analyzing optical forces at the nanoscale. Particularly, there are few reports regarding the scattering force acting on nanoscale particles, whereas the gradient force (i.e., trapping stiffness) has been reported in recent studies.[35,36] Zensen et al.[27] succeeded in evaluating the scattering force acting on Au NPs with a diameter of 80 nm using two Gaussian beams with a specialized microscopic system. They reported a scattering force on the order of 10 fN with an accuracy on the order of 1 fN, which, to the best of our knowledge, is currently the best
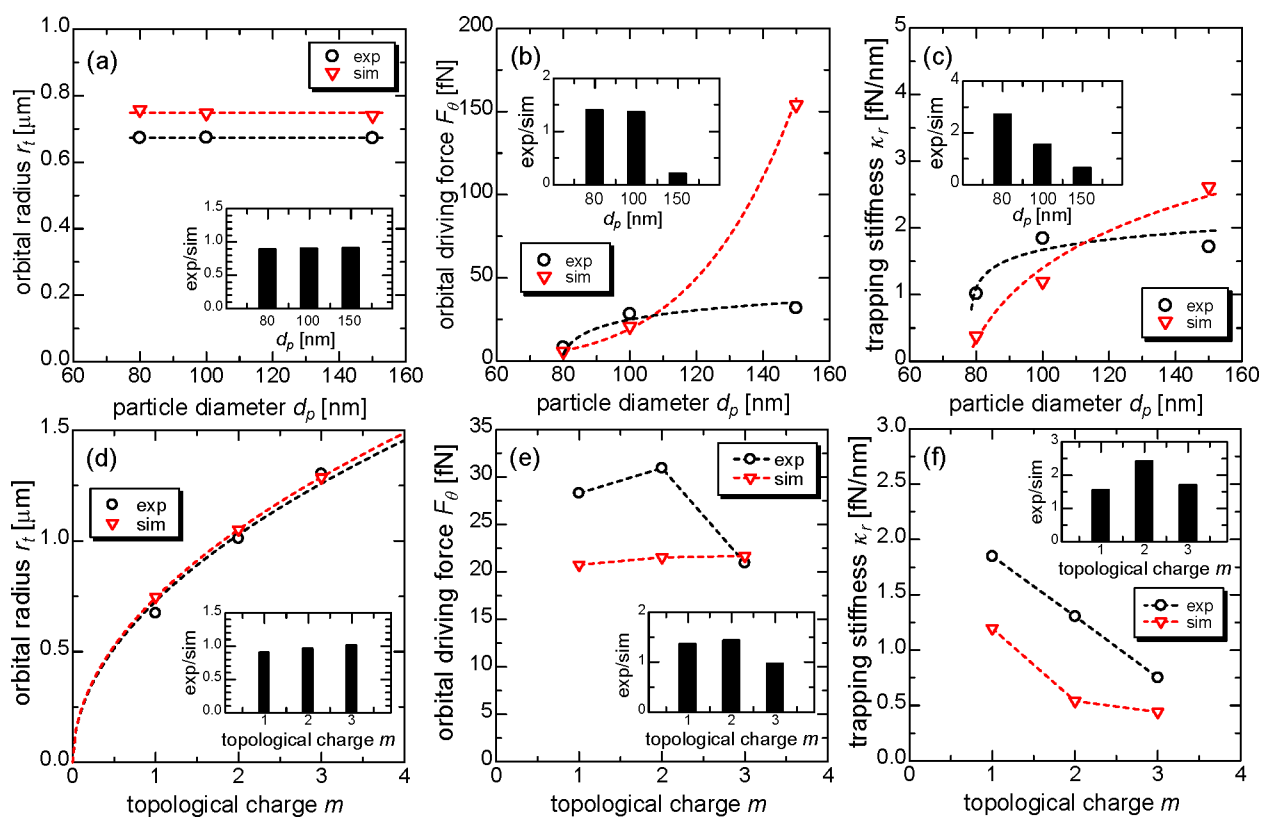
Figure 5. (a−c) Particle diameter, d_p, dependency of (a) the orbital radius r_t, (b) the tangential force F_θ, and (c) the trapping stiffness κ_r. The inset shows the ratio of each parameter for the experimental and numerical results for each d_p. The topological charge and the laser power of the incident LG beam are $m = 1$ and $L_p = 200$ mW, respectively. (d−f) Topological charge, m, dependency of (d) the orbital radius, (e) the tangential force, and (f) the trapping stiffness. The inset shows the ratio of each parameter for the experimental and numerical results for each m. The particle diameter and the laser power are $d_p = 100$ nm and $L_p = 200$ mW, respectively.

achieved accuracy. Our experimental method shows a comparable accuracy and has the advantage of simultaneously evaluating three optical components via in-plane particle tracking without a specialized microscopic setup. The validity of the experimental results is well substantiated by the consistency between the experimental and numerical results. Furthermore, the combination of the optical vortex and the nanofluidic channel results in the reproducible manipulation of the orbital motion of single Au NPs driven by a tangential force on the order of 1 fN because of the strict suppression of the forced convection in the test section. In this study, we adopted Au NPs, whose optical characteristics have been widely investigated. However, our method is applicable for investigating the optical properties, e.g., the complex refractive index, polarizability, and optical cross sections, of unknown nanomaterials.

Response of Au NPs to an Optical Vortex Field. We investigated the dependency of the optical vortex forces on the particle diameter under fixed laser irradiation conditions, as shown in Figure 5a−c. As expected, the orbital radius was independent of the particle diameter, and there was good agreement between the experimental and numerical results (Figure 5a).

Reportedly, the Rayleigh approximation can correctly describe the optical forces when the particle diameter is less than one-tenth of the wavelength of the incident light. Note that this threshold corresponds to $d_p = 100$ nm in this study. Thus, the overestimation of the tangential force for a Au NP of $d_p = 150$ nm was reasonable. When the particle diameter is larger than one-tenth of the wavelength, the Mie theory and Maxwell's stress tensor are consistent with the experimental results.[37] Dienerowitz et al.[37] reported that the Rayleigh approximation overestimates the sum of the scattering and absorption forces approximately four times larger than those calculated by the Mie theory or Maxwell's stress tensor in the case of Au NPs with the diameter of 150 nm. In our result, the Rayleigh approximation produced a tangential force that was five times larger than the experimental result; that is a reasonable discrepancy between the Rayleigh approximation and the Mie theory. Hence, we infer that the experimental results correctly represent the particle diameter dependency of the tangential force. Dienerowitz et al.[37] also reported that, for Au NPs with a diameter of 150 nm, the gradient force is almost the same between the two calculation methods. This fact indicates that the Rayleigh theory can be approximately extended to calculate the trapping stiffness even for $d_p = 150$ nm. Indeed, the experimental and numerical results agreed on the order of the trapping stiffness without a significant overestimation. In addition to the result of $d_p = 150$ nm, the experimental trapping stiffness was consistent with the numerical results with an accuracy on the order of 0.1 fN/nm.

Next, we evaluated the orbital motion of Au NPs with a diameter of 100 nm with different topological charges and a fixed laser power of $L_p = 200$ mW (Figure 5d−f). Changes in the topological charge lead to changes in the optical vortex field based on eqs 2−4. Figure 5d shows the orbital radius dependency on the topological charge. The orbital radius r_t under a topological charge m is denoted by a root of eq 2, that is, $r_t = w_0\sqrt{m/2}$. The fitted curves in Figure 5d follow the function $r_t = w_0\sqrt{m/2}$, and the experimental and numerical results were consistent with this function. Furthermore, the

orbital radius showed a good agreement between the experimental and numerical results.

The tangential-force measurement kept the accuracy between experimental and numerical results, even under different topological charges, as shown in Figure 5e. Regarding the trapping stiffness, the experimental results were qualitatively consistent with the numerical results such that a higher topological charge led to a lower trapping stiffness (Figure 5f).

In summary, our experimental method successfully evaluated the change in the optical-vortex forces due to particle size change on the order of 10 nm and indicated the difference in the interference between Au NPs and the optical vortex behind the optical-vortex manipulation. Furthermore, the experimental results demonstrated changes in the orbital motion associated with various topological charges. Particle tracking analyses in nanofluidic channels allow quantitative evaluations of the orbital radius, the tangential force, and the trapping stiffness.

■ CONCLUDING REMARKS

In this study, the orbital motion of single Au NPs driven by an optical vortex was evaluated using a nanofluidic channel optimized for suppressing the forced convection in the test section. For Au NPs with diameters of 80, 100, and 150 nm manipulated by LG beams, the gradient, scattering, and adsorption forces were quantitatively evaluated using the orbital radius, tangential force, and radial trapping stiffness. The transport phenomenon was analyzed using a Langevin dynamics simulation coupled with the Rayleigh scattering theory. We found that the simulation results reproduced the orbital motion well as functions of the laser power, particle diameter, and topological charge. The consistency between the experimental and numerical results in the Rayleigh regime indicated that our experimental method enables reliable quantitative analyses of the radial trapping stiffness (i.e., the gradient force component) and tangential force (i.e., the scattering and absorption forces) regardless of large thermal fluctuations in the Au NP dynamics. Although reliable evaluations of the scattering and absorption forces in the Rayleigh regime are challenging because of the insufficient optical force of the stable manipulation for target particles, we succeeded in analyzing scattering forces on the order of 10 fN or less with an accuracy on the order of ≈1 fN. These findings will be helpful for optical-manipulation techniques using optical vortices and other applications. In the future, the presented method will contribute to investigations of optical properties of unknown nanoscale materials via optical force analyses.

■ MATERIALS AND METHODS

Fabrication of the Nanofluidic Device. The nanofluidic device is composed of a quartz glass substrate and a polydimethyl-siloxane (PDMS) block. The glass substrate includes a nanofluidic channel pattern. During its fabrication, a photoresist reagent (ZEP520A, ZEON Corp., Japan) was spin-coated on the substrate at 3500 rpm for 40 s. The coated photoresist was baked at 180 °C for 3 min. The design of the nanofluidic channel was drawn on the photoresist using an electron beam drawing system (BEAM DRAW, Tokyo Technology) implemented in a scanning electron microscope (JSM-7200M, JEOL). The acceleration voltage and the drawing area were 30 kV and 200 × 200 μm^2, respectively.
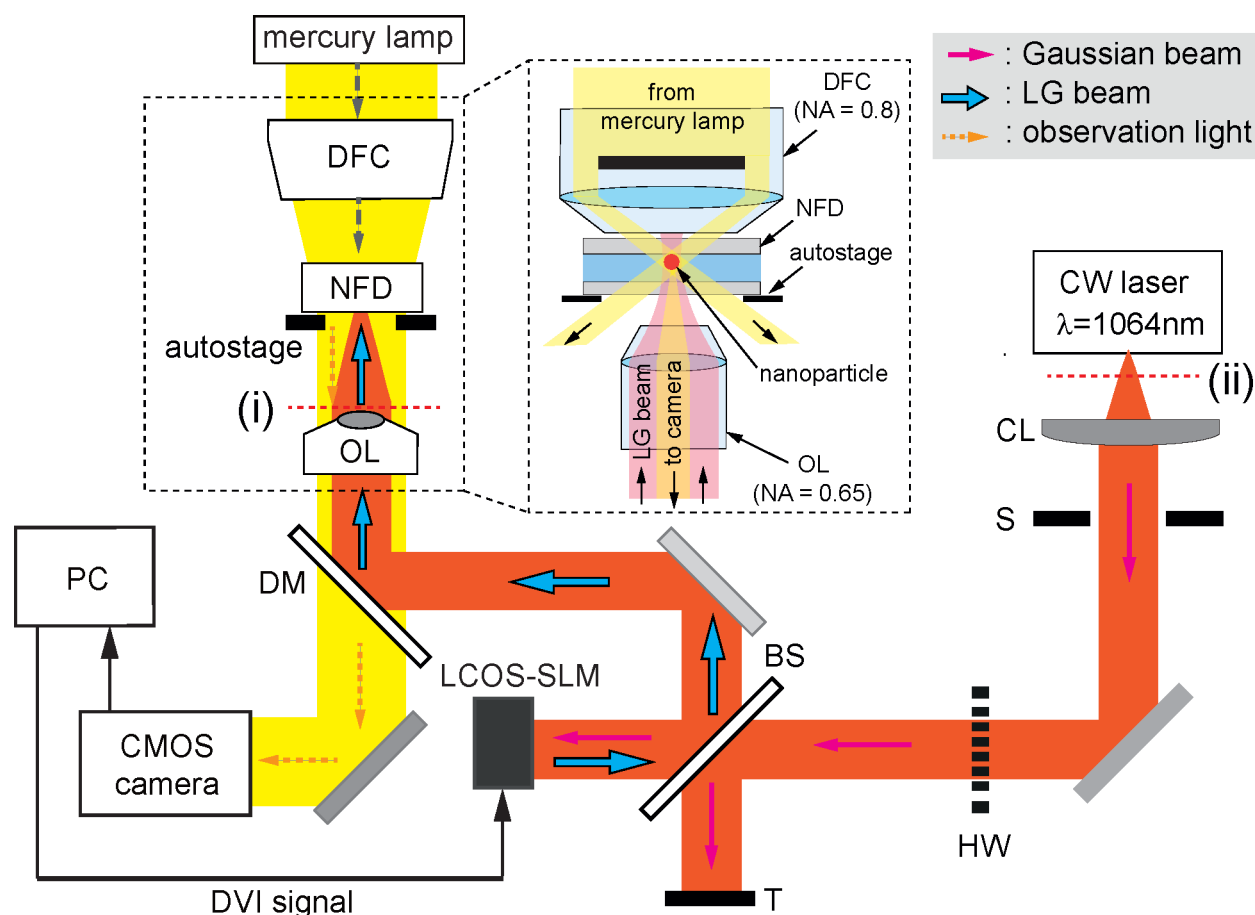
Figure 6. Schematic of the laboratory-built optical system. Abbreviations are as follows: CL, collimate lens; S, shutter; HW, half waveplate; T, terminal; BS, beam splitter; LCOS-SLM, liquid crystal on silicon-space light modulator; DM, dichroic mirror; OL, objective lens; NFD, nanofluidic device; and DFC, dark-field condenser.

The nanofluidic channel was drawn using a dosage of 62.5 μC cm^{-2}. After development, via immersion in a developer solution (ZED-N50, ZEON Corp., Japan), the nanofluidic channel was processed to a depth of 300 nm using a reactive ion etching system (RIE-10NR, Samco Inc., Japan). Trifluoromethane (CHF$_3$) gas was used as the process gas. Next, the substrate was immersed in a dimethylformamide solution overnight. Finally, the substrate was rinsed via ultrasonication in an isopropanol solution. The height of the nanofluidic channel was $\approx$300 nm. The PDMS material (Sylgard184, Dow Corning Toray Co., Ltd., Japan) was thermally cured on a mold that was fabricated as described in a previous study.[13] Holes for the inlet and outlet of the suspension were made in the PDMS block using a biopsy puncher (BP-35F, Kai Industries Co., Ltd., Japan). The glass substrate and the PDMS block were exposed to an excimer laser (SVK111R-1N1-NF0, USHIO, Japan) to modify their bonding surface to be hydrophilic and were then bonded.

Optical Setup. In the laboratory-built optical setup (Figure 6), a continuous-wave semiconductor laser with a wavelength of 1064 nm (ASF1JE01, Fitel, Furukawa Electronics, Japan) was adopted as a light source. The polarization of the Gaussian beam emitted from the laser source was aligned using a half-wave plate. Next, the beam was made incident with a liquid crystal on a silicon-space light modulator (LCOS-SLM; X13138-03, Hamamatsu Photonics K. K., Japan). Using the LCOS-SLM, the Gaussian beam was transformed into an LG

beam via spatial phase modulation. Then, the LG beam was made incident with an optical path through an inverted microscope (IX-71, Olympus, Japan) and was focused using an objective lens (LCPLN50XIR, Olympus, Japan). The LG beam irradiated the Au NPs in the nanofluidic channel, which was placed on the autostage of the inverted microscope. The Au NPs were visualized via dark-field microscopy using a mercury lamp (U-HGLGPS, Olympus, Japan) and a dark-field condenser lens with a numerical aperture of 0.8 (U-DCD, Olympus, Japan), as shown in the inset in Figure 6. The observations were recorded using a high-speed camera (Zyla, sCMOS, Andor Technology Ltd., Northern Ireland) with a frame rate of 1000 fps. In the experimental setup, the pixel size was 140 nm/pixel.

Beam Waist w_0 and Laser Power L_p. The beam waist, w_0, and the laser power, L_p, of the laboratory-built optical setup are required for the numerical simulation. To measure the beam waist, the Gaussian beam was made incident with the objective lens without spatial phase modulations. The beam profile at the focal plane was recorded by the CMOS camera. A Gaussian function was then fitted to the profile to determine the beam waist, which was defined as the distance from an optical axis to the point with a brightness value of $1/e^2$ of the maximum intensity. Figure S4a shows the acquired image of the Gaussian beam and its intensity profile, which indicates that the beam waist was $w_0 \approx 1.03$ μm.

It was necessary to measure the laser power at the focal point because the Au NPs were irradiated with the beam following energy loss along the optical path. We measured the laser power near the focal plane using an optical power meter (3A-QUAD, Ophir Ltd., Japan), as indicated by the red dotted line (i) in Figure 6 for LG beams with topological charges m in the range from 0 to 4. The measurements are shown in Figure S4b. The results indicated that the laser power increased in proportion to the set value. Additionally, the energy loss increased for higher m. Therefore, in the optical-manipulation experiment, we determined the laser power from the m and set values for each condition.

Preparation of Au NP Suspension and Infiltration of Suspension inside the Nanofluidic Channel. In this study, Au NPs with diameters of 80, 100, and 150 nm (A11-80/100/150-CIT-DIH-1-25-CS, Nanopartz, Canada) were used as target particles. First, the stock suspension was irradiated with ultrasound to disperse any preformed particle aggregates. Then, the suspension was filtrated with a membrane filter with a pore diameter of 220 nm (GSWP01300, Merck Millipore Ltd., Germany). The filtrated suspension was diluted with ultrapure water to a final concentration of the nanoparticles of 6.32×10^7 npsmL^{-1}, where nps denotes the number of nanoparticles. To mitigate the adhesion of nanoparticles to the wall of the nanofluidic channel, Triton X-100, a nonionic surfactant, was added to the suspension with the concentration of 1% (v/v). Here, the nonionic surfactant was chosen because ionic surfactants can strongly change the surface charge and dielectric property of Au NPs by attaching the particle surface.

To infiltrate the nanoparticles into the nanofluidic channel, we filled the inlet holes of the nanofluidic channel with a suspension of nanoparticles and vacuumed it for 1 min. This vacuum procedure allowed the suspension to enter the test section. The number density of the nanoparticle suspension was adjusted so that the number of nanoparticles infiltrated into the test section, estimated from the volume ratio of the test section to the whole channel, was stochastically equal to 1. Then, the test section was observed using dark-field microscopy to confirm the existence of a single nanoparticle there. If there is no particle in the test section, the nanofluidic channel was irradiated with an ultrasound to forcibly induce the nanoparticle flow inside the channel. This ultrasonication process was repeated when a single nanoparticle was observed in the test section. After infiltration of the single nanoparticle in the test section, the particle stayed during the sequential experiments, i.e., 5 h.

Langevin Dynamics Simulation Coupled with the Rayleigh Scattering Theory. The orbital motion induced by the LG beam was simulated by numerically solving the Langevin equation combined with the optical forces. We assumed an ideal in-plane orbital motion at the focal plane of the LG beam. Because the inertial term is much smaller than the drag force as a result of the tiny mass of the nanoparticle, the overdamped Langevin equation in polar coordinates $\mathbf{r} = (r, \theta)$ is acceptable as follows:

$$0 = -\xi \frac{d\mathbf{x}_p(t)}{dt} + \mathbf{F}_{opt}(\mathbf{r}) + \mathbf{F}_{rand}(t) \tag{1}$$

Here, $\mathbf{x}_p(t)$, $\mathbf{F}_{opt}(\mathbf{r})$, and $\mathbf{F}_{rand}(t)$ denote the particle position at time t, the optical forces at the position $\mathbf{r}$, and the thermal fluctuations at time t, respectively. ξ is the friction coefficient, which is $\xi = 3\pi\mu d_p$, where μ and d_p denote the viscosity and

the particle diameter, respectively. $\mathbf{F}_{opt}(\mathbf{r})$ comprises the optical gradient force, $\mathbf{F}_{grad}(\mathbf{r})$, the scattering force, $\mathbf{F}_{scat}(\mathbf{r})$, and the absorption force, $\mathbf{F}_{abs}(\mathbf{r})$. Here, because the rotational frequency of the optical vortex is much faster than that of the orbital motion of the Au NPs, we averaged the scattering and absorption forces along the azimuthal direction, resulting in an equation that is independent of the angle. Thus, the optical forces along the radial direction, $\mathbf{F}_r(r)$, and the azimuthal direction, $\mathbf{F}_\theta(r)$, are denoted as a function of $r = |\mathbf{r}|$ as follows:

$$\mathbf{F}_r(r) = \mathbf{F}_{grad}(r)$$
$$= \frac{2L_p}{\pi n_f c \epsilon_0 w_0^2} \text{Re}[\alpha^*(d_p)] \psi_m(r) \left(\frac{|m|}{r} - \frac{2r}{w_0^2} \right) \mathbf{e}_r \tag{2}$$

$$\mathbf{F}_\theta(r) = \mathbf{F}_{scat}(r) + \mathbf{F}_{abs}(r) = \frac{n_f L_p}{c w_0^2} (C_{scat} + C_{abs}) \psi_m(r) \frac{m}{kr} \mathbf{e}_\theta \tag{3}$$

Here, $n_f = 1.33$, $c = 3.00 \times 10^8$ m·s^{-1}, $\epsilon_0 = 8.85 \times 10^{-12}$ F·m^{-1}, and m denote the refractive index of water, the speed of light, the dielectric constant in a vacuum, and the topological charge of the LG beam, respectively. The beam waist, $w_0 = 1.03$ μm, and the incident laser power, L_p, are determined via experimental measurements, as described above. k and $\psi_m(r)$ are defined as

$$k = 2\pi n_f/\lambda, \ \psi_m(r) = \frac{2}{\pi|m|!} \left(\frac{\sqrt{2}\, r}{w_0} \right)^{2|m|} \exp\left(-\frac{2r^2}{w_0^2} \right) \tag{4}$$

where $\lambda = 1064$ nm is the wavelength of the incident LG beam. The polarizability of Au NPs with a diameter of d_p, $\alpha_{CM}^*(d_p)$, is given according to the Clausius–Mossotti relation as follows:

$$\alpha_{CM}^*(d_p) = \frac{\pi \epsilon_0 n_f^2 d_p^3}{2} \left(\frac{n_p^{*2} - n_f^2}{n_p^{*2} + 2n_f^2} \right) \tag{5}$$

Here, n_p^* denotes the complex reflective index of the Au NPs. In this study, we considered the interference between the incident light and secondary light radiated from the Au NPs, which results in attenuation of the incident light intensity.[38] The effect of the interference on the optical parameters was insignificant in the case of smaller particles. However, the effect becomes greater with an increase in the particle diameter; i.e., the degree of attenuation changes in a diameter-dependent manner, which can bias the change in optical forces to particle size change. Thus, the radiative correction for optical parameters of Au NPs was adopted in this study. The effect is reflected in the polarizability of the nanoparticles by correcting $\alpha_{CM}^*(d_p)$ to

$$\alpha^*(d_p) = \alpha_{CM}^*(d_p) \left(1 + i \frac{n_f^3 k_0^3 \alpha_{CM}^*(d_p)}{6\pi} \right)^{-1} \tag{6}$$

where k_0 is the wavevector in a vacuum. Based on the Rayleigh theory, the scattering cross section, C_{scat}, and the absorption cross section, C_{abs}, were determined using the relations $C_{scat} = \frac{n_f^4 k_0^4}{6\pi} |\alpha^*(d_p)|^2$ and $C_{abs} = \frac{n_f k_0}{6\pi} \text{Im}[\alpha_{CM}^*(d_p)]$, respectively.[37] The optical parameters for the numerical simulation are summarized in Table 2 for the three diameters used in this study.[39]

Table 2. Used Optical Parameters of the Au NPs with Diameters of 80, 100, and 150 nm, for the Theoretical Simulation[39a]

d_p [nm]	80	100	150
n_p^* [-]	$0.124 + 7.6i$	$0.117 + 7.6i$	$0.107 + 7.6i$
$\mathrm{Re}[\alpha^*]$ [A$^2\cdot$s^4/kg]	1.39×10^{-32}	2.71×10^{-32}	8.95×10^{-32}
C_{scat} [m^2]	2.38×10^{-16}	9.06×10^{-16}	1.01×10^{-14}
C_{abs} [m^2]	2.12×10^{-17}	3.90×10^{-17}	1.21×10^{-16}

[a]n_p^*, α^*, C_{scat}, and C_{abs} denote the complex refractive index, the polarizability with radiation reaction correction, the scattering cross section, and the absorption cross section, respectively.

The characteristics of the thermal fluctuation, $\mathbf{F}_{rand}(t)$, were defined to satisfy the Einstein's fluctuation−dissipation theorem, such that

$$\langle \mathbf{F}_{rand}(t) \rangle = 0, \quad \langle \mathbf{F}_{rand}(t_1) \cdot \mathbf{F}_{rand}(t_2) \rangle = 4\xi k_B T \delta(t_1 - t_2) \tag{7}$$

The quantity $\langle \cdot \rangle$ denotes an ensemble average; δ is the Dirac delta function; $k_B = 1.38 \times 10^{-23}$ m^2 kg s^{-2} is the Boltzmann constant; and $T = 300$ K is the absolute temperature. For discrete thermal fluctuations, the normalized random numbers, $N(t)$, were generated following a Gaussian distribution. $\mathbf{F}_{rand}(t)$ is expressed as

$$\mathbf{F}_{rand}(t) = \sqrt{\frac{4\xi k_B T}{\Delta t}} N(t) \tag{8}$$

To determine the time step in the numerical simulation, we calculated the diffusion coefficient for Au NPs with a diameter of 200 nm in two-dimensional Brownian motion with various time steps in the range from $\Delta t = 1.0 \times 10^{-6}$ s to 1.0×10^{-12} s and compared the obtained diffusion constants with the theoretical value calculated by the Stokes−Einstein equation. The result indicated that a time step of less than $\Delta t = 1.0 \times 10^{-7}$ s was sufficiently short to ignore the effect of the time step on the numerical results. Accordingly, we numerically solved eq 1 using a time step $\Delta t = 1.0 \times 10^{-7}$ s. The computational techniques used for the numerical analysis were based on our previous research,[11] which largely contributed to the high accuracy of the obtained results. Validation of the numerical scheme was also carefully made, not only from the viewpoint of computational fluid dynamics, e.g., the independence of the parameters in the iterative process, but also from that especially considering the periodicity of the phenomena in optical tweezers and the statistical characteristics of Brownian motion. The particle position at time t_i was displayed as the trajectory of the orbital motion with an interval of 1 ms, which was identical to the frame rate of the microscopic observations in the experiment.

ASSOCIATED CONTENT

ⓢ Supporting Information

The Supporting Information is available free of charge at https://pubs.acs.org/doi/10.1021/acsomega.1c04855.

> Detailed information concerning the nanofluidic channel (Figure S1), data concerning reduction of forced convection (Figure S2), data concerning evaluation of ellipticity of the particle trajectory (Figure S3), and data concerning the laboratory-built optical setup (Figure S4) (PDF)

AUTHOR INFORMATION

Corresponding Author

Satoyuki Kawano − *Graduate School of Engineering Science, Osaka University, Toyonaka, Osaka 560-8531, Japan*; Phone: +81 (6)6850 6175; Email: kawano@me.es.osaka-u.ac.jp; Fax: +81 (6)6850 6175

Authors

Kichitaro Nakajima − *Global Center for Medical Engineering and Informatics, Osaka University, Suita, Osaka 565-0871, Japan*; orcid.org/0000-0003-2644-741X

Tempei Tsujimura − *Graduate School of Engineering Science, Osaka University, Toyonaka, Osaka 560-8531, Japan*

Kentaro Doi − *Department of Mechanical Engineering, Toyohashi University of Technology, Toyohashi, Aichi 441-8580, Japan*; orcid.org/0000-0002-2663-9369

Complete contact information is available at:
https://pubs.acs.org/10.1021/acsomega.1c04855

Notes

The authors declare no competing financial interest.

ACKNOWLEDGMENTS

REFERENCES

(1) Ashkin, A.; Dziedzic, J. M. Optical levitation of liquid drops by radiation pressure. *Science* **1975**, *187*, 1073−1075.

(2) Ashkin, A. Optical trapping and manipulation of neutral particles using lasers. *Proc. Natl. Acad. Sci. U.S.A.* **1997**, *94*, 4853−4860.

(3) Ashkin, A.; Dziedzic, J. M. Internal cell manipulation using infrared laser traps. *Proc. Natl. Acad. Sci. U.S.A.* **1989**, *86*, 7914−7918.

(4) Arima, A.; Harlisa, I. H.; Yoshida, T.; Tsutsui, M.; Tanaka, M.; Yokota, K.; Tonomura, W.; Yasuda, J.; Taniguchi, M.; Washio, T.; Okochi, M.; Kawai, T. Identifying single viruses using biorecognition solid-state nanopores. *J. Am. Chem. Soc.* **2018**, *140*, 16834−16841.

(5) Kondylis, P.; Zhou, J.; Harms, Z. D.; Kneller, A. R.; Lee, L. S.; Zlotnick, A.; Jacobson, S. C. Nanofluidic devices with 8 pores in series for real-time, resistive-pulse analysis of hepatitis B virus capsid assembly. *Anal. Chem.* **2017**, *89*, 4855−4862.

(6) Yusko, E. C.; Bruhn, B. R.; Eggenberger, O. M.; Houghtaling, J.; Rollings, R. C.; Walsh, N. C.; Nandivada, S.; Pindrus, M.; Hall, A. R.; Sept, D.; Li, J.; Kalonia, D. S.; Mayer, M. Real-time shape approximation and fingerprinting of single proteins using a nanopore. *Nat. Nanotechnol.* **2017**, *12*, 360−367.

(7) Sen, Y.-H.; Jain, T.; Aguilar, C. A.; Karnik, R. Enhanced discrimination of DNA molecules in nanofluidic channels through multiple measurements. *Lab Chip* **2012**, *12*, 1094−1101.

(8) Fukuyama, T.; Nakama, S.; Maeda, Y. T. Thermal molecular focusing: tunable cross effect of phoresis and light-driven hydro-dynamic focusing. *Soft Matter* **2018**, *14*, 5519−5524.

(9) Doi, K.; Takeuchi, H.; Nii, R.; Akamatsu, S.; Kakizaki, T.; Kawano, S. Self-assembly of 50 bp poly(dA)-poly(dT) DNA on highly oriented pyrolytic graphite via atomic force microscopy observation and molecular dynamics simulation. *J. Chem. Phys.* **2013**, *139*, 085102.

(10) Qian, W.; Doi, K.; Kawano, S. Effects of polymer length and salt concentration on the transport of ssDNA in nanofluidic channels. *Biophys. J.* **2017**, *112*, 838−849.

(11) Nagura, R.; Tsujimura, T.; Tsuji, T.; Doi, K.; Kawano, S. Coarse-grained particle dynamics along helical orbit by an optical vortex irradiated in photocurable resins. *OSA Continuum* **2019**, *2*, 400−415.

(12) Nito, F.; Shiozaki, T.; Nagura, R.; Tsuji, T.; Doi, K.; Hosokawa, C.; Kawano, S. Quantitative evaluation of optical forces by single particle tracking in slit-like microfluidic channels. *J. Phys. Chem. C* **2018**, *122*, 17963−17975.

(13) Tsuji, T.; Nakatsuka, R.; Nakajima, K.; Doi, K.; Kawano, S. Effect of hydrodynamic inter-particle interaction on the orbital motion of dielectric nanoparticles driven by an optical vortex. *Nanoscale* **2020**, *12*, 6673−6690.

(14) Ashkin, A. Forces of a single-beam gradient laser trap on a dielectric sphere in the ray opticas regime. *Biophys. J.* **1992**, *61*, 569−582.

(15) Nakajima, K.; Nakatsuka, R.; Tsuji, T.; Doi, K.; Kawano, S. Synchronized resistive-pulse analysis with flow visualization for single micro- and nanoscale objects driven by optical vortex in double orifice. *Sci. Rep.* **2021**, *11*, 9323.

(16) Nakatsuka, R.; Yanai, S.; Nakajima, K.; Doi, K.; Kawano, S. Electrical sensing of Au nanoparticles manipulated by an optical vortex. *J. Phys. Chem. C* **2021**, *125*, 9507−9515.

(17) Allen, L.; Beijersbergen, M. W.; Spreeuw, R. J. C.; Woerdman, J. P. Orbital angular momentum of light and the transformation of Laguerre-Gaussian laser modes. *Phys. Rev. A* **1992**, *45*, 8185−8189.

(18) Barnett, S. M.; Allen, L. Orbital angular momentum and nonparaxial light beams. *Opt. Commun.* **1994**, *110*, 670−678.

(19) Courtial, J.; Dholakia, K.; Allen, L.; Padgett, M. Gaussian beams with very high orbital angular momentum. *Opt. Commun.* **1997**, *144*, 210−213.

(20) O'Neil, A. T.; Padgett, M. J. Three-dimensional optical confinement of micron-sized metal particles and the decoupling of the spin and orbital angular momentum within an optical spanner. *Opt. Commun.* **2000**, *185*, 139−143.

(21) Toyoda, K.; Takahashi, F.; Takizawa, S.; Tokizane, Y.; Miyamoto, K.; Morita, R.; Omatsu, T. Transfer of light helicity to nanostructures. *Phys. Rev. Lett.* **2013**, *110*, 143603.

(22) Toyoda, K.; Miyamoto, K.; Aoki, N.; Morita, R.; Omatsu, T. Using optical vortex to control the chirality of twisted metal nanostructures. *Nano Lett.* **2012**, *12*, 3645−3649.

(23) Li, M.; Yan, S.; Yao, B.; Liang, Y.; Lei, M.; Yang, Y. Optically induced rotation of Rayleigh particles by vortex beams with different states of polarization. *Phys. Lett. A* **2016**, *380*, 311−315.

(24) Li, M.; Yan, S.; Yao, B.; Liang, Y.; Zhang, P. Spinning and orbiting motion of particles in vortex beams with circular or radial polarizations. *Opt. Express* **2016**, *24*, 20604−20612.

(25) Zhao, Y.; Edgar, J. S.; Jeffries, G. D. M.; McGloin, D.; Chiu, D. T. Spin-to-orbital angular momentum conversion in a strongly focused optical beam. *Phys. Rev. Lett.* **2007**, *99*, 073901.

(26) Saito, K.; Okubo, S.; Kimura, Y. Change in collective motion of colloidal particles driven by an optical vortex with driving force and spatial confinement. *Soft Matter* **2018**, *14*, 6037−6042.

(27) Zensen, C.; Villadsen, N.; Winterer, F.; Keiding, S. R.; Lohmüller, T. Pushing nanoparticles with light A femtonewton resolved measurement of optical scattering forces. *APL Photonics* **2016**, *1*, 026102.

(28) Thalhammer, G.; Obmascher, L.; Ritsch-Marte, M. Direct measurement of axial optical forces. *Opt. Express* **2015**, *23*, 6112−6129.

(29) Roichman, Y.; Sun, B.; Stolarski, A.; Grier, D. G. Influence of nonconservative optical forces on the dynamics of optically trapped colloidal spheres: The fountain of probability. *Phys. Rev. Lett.* **2008**, *101*, 128301.

(30) Chen, M.; Mazilu, M.; Arita, Y.; Wright, E. M.; Dholakia, K. Dynamics of microparticles trapped in a perfect vortex beam. *Opt. Lett.* **2013**, *38*, 4919−4922.

(31) Ferrara, L.; Baldini, E.; Minzioni, P.; Bragheri, F.; Liberale, C.; Fabrizio, E. D.; Cristiani, I. Experimental study of the optical forces exerted by a Gaussian beam within the Rayleigh range. *Journal of Optics* **2011**, *13*, 075712.

(32) Villadsen, N.; Andreasen, D. Ø.; Hagelskjær, J.; Thøgersen, J.; Imparato, A.; Keiding, S. R. Pushing the limit: investigation of hydrodynamic forces on a trapped particle kicked by a laser pulse. *Opt. Express* **2015**, *23*, 13141−13152.

(33) Catala, F.; Marsa, F.; Montes-Usategui, M.; Farre, A.; Martin-Badosa, E. Extending calibration-free force measurements to optically-trapped rod-shaped samples. *Sci. Rep.* **2017**, *7*, 42960.

(34) Xu, T.; Wu, S.; Jiang, Z.; Wu, X.; Zhang, Q. Video microscopy-based accurate optical force measurement by exploring a frequency-changing sinusoidal stimulus. *Appl. Opt.* **2020**, *59*, 2452−2456.

(35) Purohit, P.; Samadi, A.; Bendix, P. M.; Laserna, J. J.; Oddershede, L. B. Optical trapping reveals differences in dielectric and optical properties of copper nanoparticles compared to their oxides and ferrites. *Sci. Rep.* **2020**, *10*, 1198.

(36) Jiang, Q.; Claude, J.-B.; Wenger, J. Plasmonic nano-optical trap stiffness measurements and design optimization. *Nanoscale* **2021**, *13*, 4188−4194.

(37) Dienerowitz, M.; Mazilu, M.; Dholakia, K. Optical manipulation of nanoparticles: a review. *J. Nanophotonics* **2008**, *2*, 21875.

(38) Draine, B. T. The discrete-dipole approximation and its application to interstellar graphite grains. *Astrophys. J.* **1988**, *333*, 848.

(39) Ordal, M. A.; Long, L. L.; Bell, R. J.; Bell, S. E.; Bell, R. R.; Alexander, R. W.; Ward, C. A. Optical properties of the metals Al, Co, Cu, Au, Fe, Pb, Ni, Pd, Pt, Ag, Ti, and W in the infrared and far infrared. *Appl. Opt.* **1983**, *22*, 1099−1119.